Atomic-scale dynamical structures of fatty acid bilayers observed by ultrafast electron crystallography

Songye Chen, Marco T. Seidel, and Ahmed H. Zewail†

Laboratory for Molecular Sciences, Noyes Laboratory of Chemical Physics, California Institute of Technology, Pasadena, CA 91125

Contributed by Ahmed H. Zewail, May 13, 2005

The structure and dynamics of a biological model bilayer are reported with atomic-scale resolution by using ultrafast electron crystallography. The bilayer was deposited as a Langmuir-Blodgett structure of arachidic (eicosanoic) fatty acids with the two chains containing 40 carbon atoms (≈50 Å), on a hydrophobic substrate, the hydrogen terminated silicon(111) surface. We determined the structure of the 2D assembly, establishing the orientation of the chains and the subunit cell of the CH_2 distances: a_0 = 4.7 Å, b_0 = 8.0 Å, and c_0 = 2.54 Å. For structural dynamics, the diffraction frames were taken every 1 picosecond after a femtosecond temperature jump. The observed motions, with sub-Å resolution and monolayer sensitivity, clearly indicate the coherent anisotropic expansion of the bilayer solely along the aliphatic chains, followed by nonequilibrium contraction and restructuring at longer times. This motion is indicative of a nonlinear behavior among the anharmonically coupled bonds on the ultrashort time scale and energy redistribution and diffusion on the longer time scale. The ability to observe such atomic motions of complex structures and at interfaces is a significant leap forward for the determination of macromolecular dynamical structures by using ultrafast electron crystallography.

dynamics | ultrafast electron diffraction | Langmuir-Blodgett films

Membranes of bilayers are an essential part of biological structures and are model systems for behavior on surfaces and at interfaces (1–3). Even though there exists a rich literature about the structure and spectroscopy of membranes (4–6) and their function in biological environments, very little is known about their dynamical structures on the ultrashort time scale. Because the atomic motions on these time scales are critical to the subsequent global changes responsible for the biological function (7), it is essential to elucidate the primary dynamical behavior of the structures in the nonequilibrium regime and with atomic-scale resolution. The combined spatial and temporal resolutions of the recently developed ultrafast electron crystallography (UEC) (8–10) make the methodology ideal for determining dynamical structures of nanometer-scale (2D) bilayers, but the challenges are numerous.

As a step in this direction, we studied a bilayer of fatty acids deposited on a hydrophobic surface substrate, invoking the well known Langmuir-Blodgett (LB) technique. It allows for a controlled layer-by-layer deposition of ordered molecular films and has been used to create model biological membranes for studies under controlled conditions (11, 12). Although biomembranes are more complicated by the presence of intercalaters, the LB bilayers represent the building blocks of lipid bilayers, in our case with the molecular chains extending up to ≈50 Å. LB films themselves are of considerable interest in various areas of research involving self-assembly and self-organization and in technology developments such as molecular electronics and nonlinear optics.

Previous static diffraction studies have provided patterns and analyses with focus on the distances between the ions (x-ray) and in thick films of many layers (11–15). In these investigations, however, the structures were not time-resolved and were not directly reflective of the influence of the supporting surface. Femtosecond time-resolved studies (16) of biomembranes have examined the spectroscopy of local probes, and time-resolved x-ray diffraction studies have elucidated the laser-induced disorder above the damage threshold of the organic film (17). In the former study the structure cannot be determined, and for the latter the film was 83 layers and it was not possible to solve for the structure of the fatty acid assembly. The laser heating resulted in a destructive change above the damage threshold.

Here, we report direct determination of the structure and dynamics of one bilayer of arachidic (eicosanoic) fatty acid (two of $C_{19}H_{39}COOH$). With the UEC sensitivity and resolution, we determined the structure, thus establishing the orientation of the aliphatic chains and obtaining the subunit cell molecular $–CH_2–CH_2–$ dimensions; Fig. 1 displays the structure of the bilayer studied and the subunit cell in two directions. We also present the observation of the coherent and anisotropic dynamical expansion in the bilayer structure and the restructuring toward equilibration at longer times. The time scales involved after the femtosecond temperature jump are reported from the diffraction frames taken every 1 ps. From these studies a structural dynamics picture emerges for the bilayer on the substrate and for its atomic motions.

Methodology

UEC. The experiments were carried out in our UEC apparatus, which in part consists of three connected ultrahigh vacuum chambers: sample preparation, load-lock, and scattering chamber. The apparatus also has a femtosecond laser system used for the heating pulse and the generation of the ultrafast electron packet (8–10, 18). In our experiments, the IR laser pulses (800 nm, ≈100 fs, ≈1 mJ, 1 kHz repetition rate) served as the heating pulses and were focused onto the sample surface at an incidence angle of 30° and area of illumination of 1.3 mm^2. A weaker beam was split from the IR beam, frequency-tripled (266 nm, ≈10 nJ), and focused onto a back-illuminated silver photocathode after an adjustable time delay Δt to generate the electron pulses [300 fs to a few ps, depending on density (8, 18)] via the photoelectric effect. A series of deflectors and apertures were used to guide the electron beam to a grazing incidence on the sample, adjustable from θ_i = 0–5°. The diffraction patterns were recorded with a low-noise, image-intensified, charge-coupled device camera assembly capable of single-electron detection.

Conceptually, the methodology is as follows (Fig. 2). The heating IR laser pulse is used to initiate the structural change, which is then probed by the electron pulse. The electrons with energy of 30 keV and de Broglie wavelength $\lambda_{\text{de Broglie}}$ of 0.07 Å impinges at a grazing incidence angle θ_i onto the surface and

Freely available online through the PNAS open access option.

Abbreviations: UEC, ultrafast electron crystallography; LB, Langmuir-Blodgett.

†To whom correspondence should be addressed. E-mail: zewail@caltech.edu.

www.pnas.org/cgi/doi/10.1073/pnas.0504022102

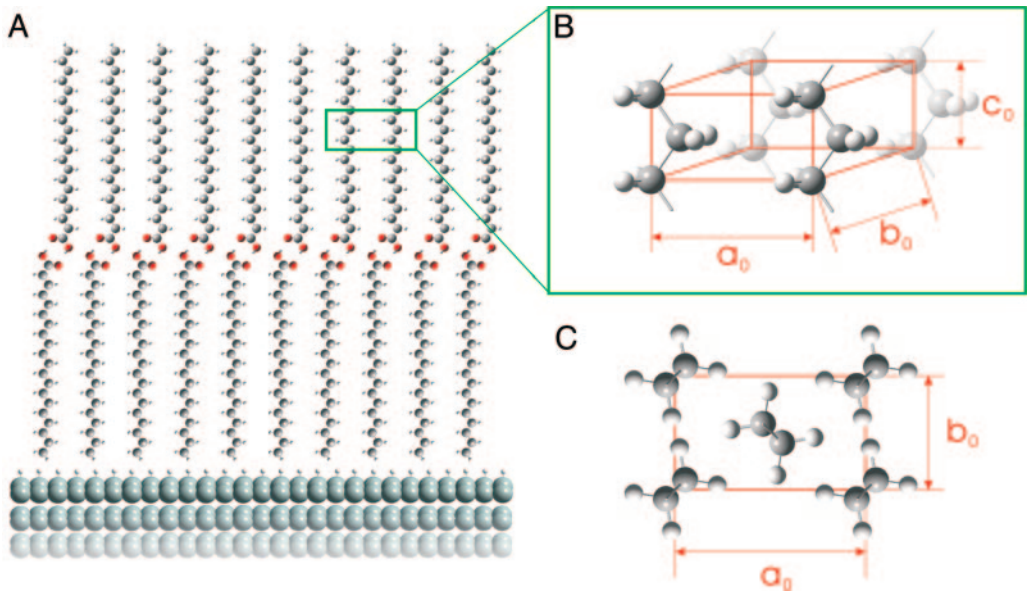

Fig. 1. Structure of the fatty acid LB bilayer. (*A*) Schematic side view of the arachidic acid bilayer on hydrogen-terminated Si(111). (*B*) Orthorhombic CH_2 subunit cell of aliphatic chains with lattice parameters a_0, b_0, and c_0. For clarity the center chain is not shown. (*C*) Top view of the orthorhombic subunit cell with lattice parameters a_0 and b_0.

scatters to form the diffraction pattern in the far field. The zero of time was determined *in situ*.

The bilayer substrate was mounted on a goniometer, allowing positioning of the sample in three translational and two rotational degrees of freedom (precision in x, y, and z is 10 μm and in θ, ϕ is 0.01°). All experiments were carried out under ultrahigh vacuum conditions (pressure $\approx 10^{-10}$ Torr) and at room temperature. Because of the low-electron flux ($\approx$1 pA/mm^2), there is no damage or charging of the LB bilayer, as is evident from the fact that no change or deterioration in the quality of the diffraction patterns were observed over the entire course of our experiment.

Bilayer Preparation. The fatty acids were deposited on the hydrogen-terminated silicon in the form of a bilayer in a so-called Y-geometry, i.e., the carboxylic functions are facing each other, to form the two layers. The bilayer is attached to the surface by its hydrophobic tail (see Fig. 1*A*). The Si(111) substrate was hydrogen-terminated before deposition by standard methods (8). The deposition took place in a LB-dipping trough at a dipping pressure of 10 mN/m. The used subphase was a diluted water/NaOH/$CaCl_2$ solution (c[NaOH] = 10^{-2} mmol/liter, c[$CaCl_2$] = 0.5 mmol/liter) at pH $\approx$9. Some calcium ions are present in the bilayer; however, in this study our focus is on the CH_2 distances, as they represent a real challenge for their molecular importance and the relatively lower scattering cross section compared with ions. We note that the substrate used here is not characterized by surface-dipole layers, which could deflect the beam, as in some oxide films (19).

The deposition along the dipping direction is the [11$\bar{2}$] direction of silicon. Two different orientations are distinguishable: parallel and perpendicular to the dipping direction, which are the [11$\bar{2}$] and [$\bar{1}$10] directions of silicon, respectively. These two distinct directions correspond to the azimuthal angle $\phi = 0°$ and $\phi = 90°$, respectively. Depending on θ_i, we can clearly see distinct diffraction patterns of the bilayer or the substrate, as shown below.

Results and Discussion

The observed diffraction pattern is determined by the structure at a time t with respect to the heating pulse at t_0. By varying the time delay, $\Delta t = t - t_0$, a series of diffraction frames can be obtained as a function of time. In each frame, the Bragg spots and streaks represent the reciprocal lattice of the structure in real space; the positions provide the symmetry and unit cell dimensions and intensities give the arrangements within the unit cell. The important parameters are the momentum transfer $\vec{s}$, the angle of incidence θ_i, and the azimuthal angle ϕ (see Fig. 2 *B* and *C*). Hence, three sets of experiments were carried out. First, structural analysis was made from the frames that display the Bragg spots and streaks in s-space; second, the rocking curve was obtained by observing the change of the diffracted intensities with different θ_i and ϕ; and finally, we obtained frames of diffraction as a function of time for a given θ_i and ϕ and monitored changes in position, intensity, and width of diffraction peaks.

Structural Determination. The static diffraction patterns obtained with the ultrashort electron pulses at different incidence angle θ_i and azimuthal angle ϕ, but without the heating pulses, are shown in Fig. 3. All diffraction patterns are composed of spots (and streaks), showing the high quality of the crystalline structure of the arachidic acid bilayer and the underlying hydrogen terminated Si(111) surface. The diffraction patterns at low incidence angle of the electrons ($\theta_i = 0.8°$) parallel ($\phi = 0°$) and perpendicular ($\phi = 90°$) to the dipping direction are shown in Fig. 3 *A* and *B*, respectively. At this angle of incidence the diffraction patterns resulting from the bilayer molecules are very clear, consistent with the penetration depth of the electrons being very small (nanometers compared to the penetration depth of $\approx$16 μm for the heating pulse). At higher incidence angle ($1° < \theta_i < 5°$), however, additional diffraction Bragg spots appear, resulting from the single crystal silicon substrate. Fig. 3*C* shows a diffraction pattern at $\phi = 1°$ off the zone axis [11$\bar{2}$] of silicon. The observed diffraction patterns of the bilayer take the form of rectangular arrays of spots, as readily seen in Fig. 3 *A* and *B*. The spots are elongated into streaks along the direction normal to the shadow edge, because of the 2D nature of the bilayer. The restriction in the direction normal to the substrate interface in real space is shown as elongation in reciprocal space.

The diffraction patterns are indexed from the positions of the

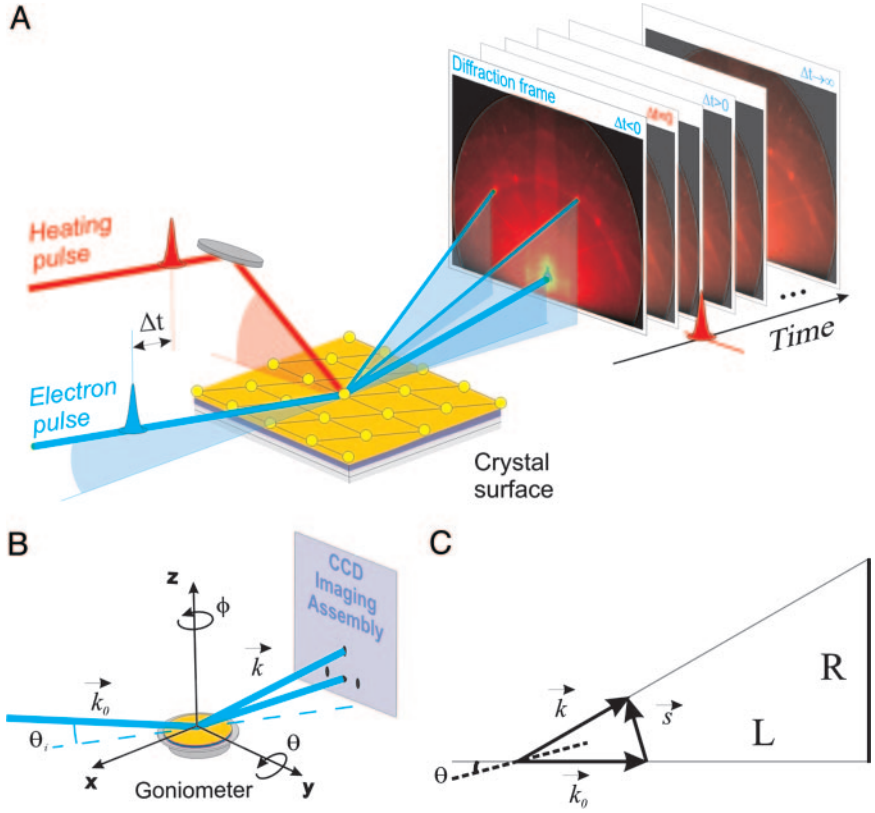

Fig. 2. Methodology of UEC. (*A*) Schematic view of the experiment, showing the heating and electron pulses, together with typical diffraction frames. (*B*) Geometry of experiment, where $\vec{k}_0$ is the wave vector of the incident electron beam, $\vec{k}$ is that of the diffracted beam forming the Bragg spots; $k = |\vec{k}_0| = |\vec{k}| = 1/\lambda$. The direction of the incident electron beam is defined with respect to a specific crystal orientation (zone axis). θ_i is the incidence angle between the electron beam and the sample surface, and ϕ is the angle between the projection of the electron beam on the sample surface and the zone axis, which is Si[11$\bar{2}$] in these experiments. (*C*) Kinematics of the electron scattering. The momentum transfer $\vec{s} \equiv \vec{k} - \vec{k}_0$ in reciprocal space satisfies the Laue condition $\vec{s} = h\vec{a}^* + k\vec{b}^* + l\vec{c}^*$, where integers h, k, and l are the Miller indices, and $\vec{a}^*$, $\vec{b}^*$, and $\vec{c}^*$ are reciprocal lattice constants. The value of $s = |\vec{s}|$ is given by $s = 2k \sin(\theta)$, and $\tan(2\theta) = R/L$, where R is the distance between the diffraction spot and the main beam position on the screen and L is the distance between the sample and the screen, i.e., the camera length. When the diffracted angle θ is very small, $\sin(\theta) = \theta$ and $\tan(2\theta) = 2\theta$, and the momentum transfer is simply $k \cdot R/L$.

spots as shown in Fig. 3 *A–C*. In principle, the long aliphatic chains pack with their chain axes parallel to each other but not necessarily perpendicular to the substrate surface. The C_2H_4 units form a sublattice with three possible different symmetries: orthorhombic, monoclinic, or triclinic (20). There are a number of possible variations of the subcell structure depending on the relative displacement of adjacent molecules, labeled by Miller indices of the interface layers. These different arrangements can be uniquely determined by the measured lattice parameters and patterns that display systematic absences of certain spots (13, 15). The main cell can also be established for the fatty acid bilayers and has the same dimensions in the plane perpendicular to the chain direction. Along the chains we observe diffraction of the C_2H_4 subunits; the main cell in this direction has a much smaller *s*-value.

From the diffraction frames at negative times, or in the absence of the heating pulse, the subunit cell parameters of the bilayer were directly determined to be $a_0 = 4.7$ Å and $b_0 = 8.0$ Å (from the side spacing between the Bragg spots) and $c_0 = 2.54$ Å (from the vertical *s*-spacing); the symmetry of the bilayer is an orthorhombic R(001) packing, with the (001) plane parallel to the Si(111) surface. The uncertainties in the determined absolute lattice constants are ≈3%, mostly resulting from the uncertainty in the camera length of ≈2%. However, it should be pointed out that these uncertainties are for the absolute values and do not affect the changes measured for the time-resolved results. The monitored changes in the peak positions were clear and robust as shown below in the diffraction difference frames.

The experimental values obtained here for the lattice parameters within the plane differ from the predicted theoretical values of $a_0 = 4.96$ Å and $b_0 = 7.4$ Å (20). The difference can be explained by the fact that the theoretical values were calculated for infinite aliphatic chains and do not take into account the carboxylic end group of fatty acids. Moreover the bilayer consists only of two monolayers, so the substrate (21) and the deposition conditions [e.g., the dipping pressure (15) or the pHs of the solution (22)] all have an important role in the order at the interface. The spacing c_0 between CH_2 planes agrees very well with the theoretical value of 2.54 Å, as it represents separation between strong C—C bonds.

Rocking Curves. The rocking curves (θ_i changes) give insight into the overall order of the bilayer, and similarly the ϕ changes. First, the diffraction patterns show a distinct behavior with the azimuthal angle ϕ. The patterns do not change considerably when rotated in a range of ±14° about ϕ both parallel as well as perpendicular to the dipping direction. The Bragg spots remain at their positions as shown in Fig. 3 *A* and *B*; only the intensities undergo a small change. Further increase of the angle ϕ results in extension of the Bragg spots into lines parallel to the shadow edge. This behavior is in vast contrast to the change of the diffraction patterns of the single crystal Si(111) surface (23). Second, the diffraction patterns of the bilayer do not change

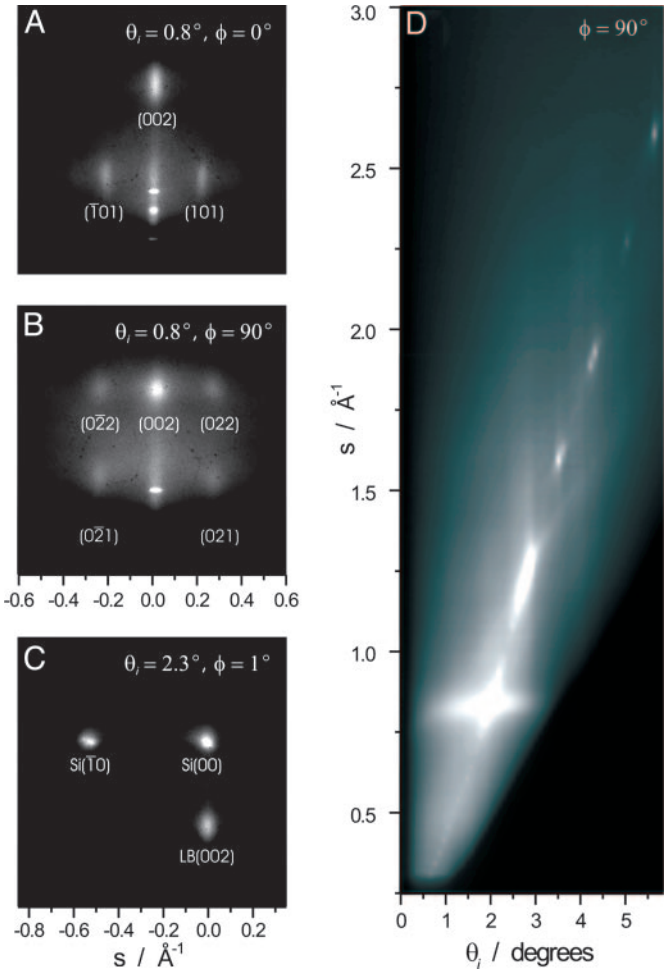

Fig. 3. Diffraction patterns and the rocking curve. (*A–C*) Experimentally observed diffraction patterns of the fatty acid arachidic LB bilayer with the indexing indicated for an orthorhombic R(001) structure. (*A*) Diffraction pattern for the bilayer at $\theta_i = 0.8°$ and $\phi = 0°$. The *s* range is from −0.6 to +0.6 Å^{-1} in the horizontal direction and from 0 to +1.2 Å^{-1} in the vertical direction. (*B*) $\theta_i = 0.8°$ and $\phi = 90°$. The *s* range is the same as in A. (*C*) $\theta_i = 2.3°$ and $\phi = 1°$. The *s* range is from −0.85 to +0.35 Å^{-1} in the horizontal direction and from +0.45 to +1.65 Å^{-1} in the vertical direction. The Bragg spots of silicon are indexed in terms of the (111) surface in the zone axis of [11$\bar{2}$]. At this angle Si(00) can also be indexed in terms of the bulk structure as Si(444). (*D*) Experimental rocking curve for the *z*-component of scattering vector *s* (from +0.25 to +3.0 Å^{-1}) vs. incidence angle θ_i (0–5.85°) at $\phi = 90°$, showing the (002)peak (see diffraction near $s = 0.8$ Å^{-1}) of the bilayer and (00)peak of the Si(111) surface (at higher *s*-values). Note that for small θ_i (*A* and *B*) the diffraction is that of the bilayer.

substantially with different incidence angle θ_i. Fig. 3*D* gives the positions of the LB(002) peak and the Si(00) peak as a function of θ_i parallel to the dipping direction. It is clear, that while the LB(002) peak remains at the same *s* position the Si(00) peak position changes periodically with θ_i, showing the higher orders of the (111)Bragg diffraction.

These observations indicate a significant coherence length (nanometers) along the fatty acid chains. From the patterns and their changes with θ_i and ϕ we establish that these chains are perpendicular to the substrate. Moreover, the striking order of the bilayer at the interface, which is reflected in the high-quality and structured diffraction patterns observed here, is indicative of a 2D crystalline structure but with unique dynamical anisotropy, as discussed below. In our study, the condition for bilayer drawing from the trough is similar to that reported in studies using atomic force microscopy (22), and the results are entirely consistent with the perfect layering caused by the inability to convert between different phases at high pHs.

Structural Dynamics. To study dynamics of the structured bilayer, the diffraction patterns were followed as a function of time after the temperature jump. At negative time delays, i.e., when the electrons arrive before the laser pulses, the diffraction frames are the same as the static diffraction pattern. These frames serve as reference patterns for the subsequent changes with time. Fig. 4*A* shows the time-dependent diffraction difference frames, with respect to the diffraction pattern before time zero, for recording in the dipping direction and at low incidence angle ($\theta_i = 0.8°$, $\phi = 0°$). As expected, the diffraction difference frame at negative time delay (−20 ps) does not show any features, i.e., there is no change before time zero. Immediately after the heating pulse (0 and 1 ps), an intensity loss of the Bragg spots is observed, as dark spots appear in the difference frames. The change in the Bragg spots becomes more prominent over time (10–100 ps). The lower part of the peaks becomes brighter, whereas the upper part becomes darker, showing a downward shift of the Bragg spots. With extended time delays (200–1,110 ps), the difference patterns get fainter again, indicating that the peaks are moving back to their original position. This behavior confirms that both the heating and electron pulses, because of their ultrashort durations and fluxes, do not damage the bilayer. It should be emphasized that the structural change is observed only in a direction perpendicular to the shadow edge of the diffraction pattern, i.e., in the vertical direction of the momentum transfer *s*-coordinate. A similar behavior is observed for all diffraction of the bilayer regardless of ϕ and θ_i.

To quantify the change, each Bragg spot, which was found to fit well to a Voigt line shape function in the vertical direction, provided us with the precise center position, line width, and intensity as a function of time. Care was taken to subtract the background, which results mainly from incoherent, inelastic, and other scatterings. The time-dependent peak shift of the Bragg spots in the vertical direction compared with their original position is depicted in Fig. 4*B* as the *z*-component of the momentum transfer *s* versus delay time, for $\phi = 90°$ and $\theta_i = 0.8°$. As is readily seen, the five Bragg spots all move down and then come back with similar time dependencies. However, there is a relatively small difference between the spots with Miller indices $l = 1$ [e.g., (0$\bar{2}$1) and (021)] and $l = 2$ [e.g., (0$\bar{2}$2), (002), and (022)]. The possible reason for this difference is the movement of the atoms in different lattice planes.

A change of the center position of a Bragg spot in reciprocal space represents a change in lattice spacing in real space; the peaks moving down indicate an expansion of the lattice in the direction perpendicular to the interface. Therefore, we converted the peak shift into real space, and the resulting change in lattice spacing Δc_0 is plotted against time in Fig. 5*A*. The plot shows an ultrafast rise of Δc_0, followed by a slower decay. This behavior represents an initial expansion of the subcell in the bilayer after impulsive laser-pulse heating of the substrate followed by a subsequent compression caused by the heat dissipation. Within our resolution, no change in lattice spacing is observed in the plane perpendicular to the normal. The absolute change Δc_0 is 0.10 and 0.05 Å in the diffraction orders with $l = 1$ and $l = 2$, respectively. For $l = 1$, the change is 4% of the static value $c_0 = 2.54$ Å. For the same *l*, the expansion of the bilayer takes place with a time constant of 25 ps, whereas the subsequent compression occurs with 55 ps. For all peaks, the much longer time behavior is well described with a restructuring time constant of 1.15 ns. For the other spots the behavior is similar, and the difference in amplitude of change in Δc_0 reflects the different orders of diffraction.

To compare the structural dynamics in the bilayer with that in

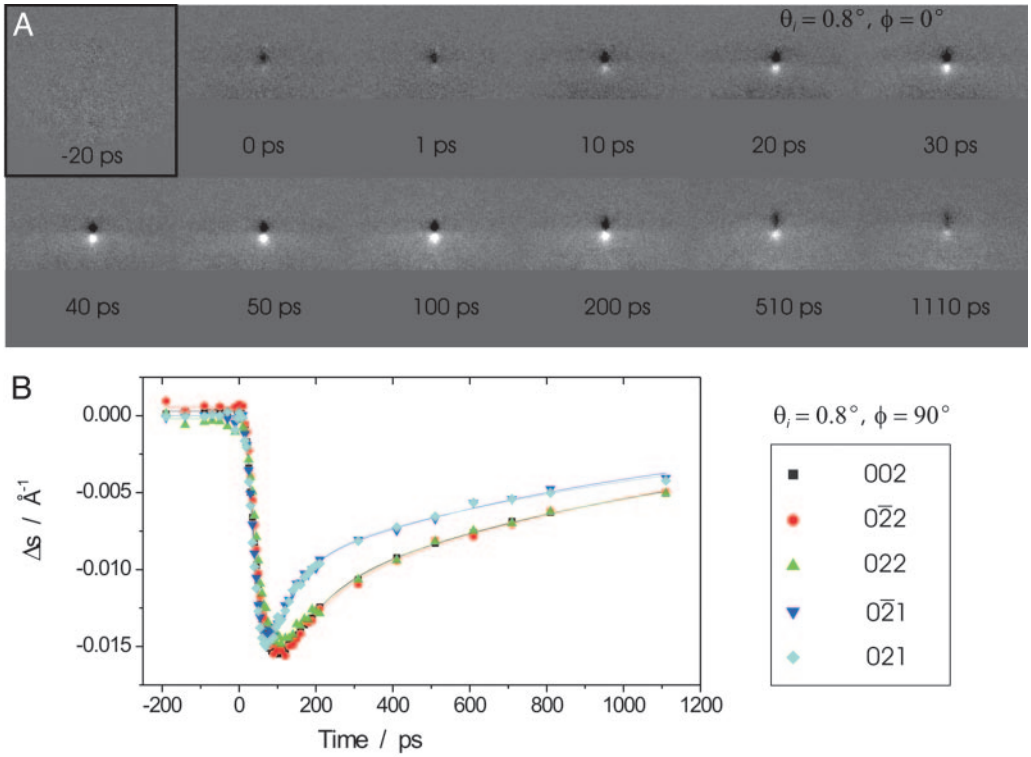

Fig. 4. The time-dependent diffraction of the bilayer. (*A*) The diffraction frame difference at various time delays obtained for the (002) Bragg spot at $\theta_i = 0.8°$ and $\phi = 0°$. Note the absence of diffraction in the frame difference at negative time, the appearance at 1 ps, and fading again at long times. (*B*) The *z*-component change Δs of the momentum transfer as a function of time for the Bragg spots in the diffraction patterns obtained at $\theta_i = 0.8°$ and $\phi = 90°$. Similar behavior was observed for all diffractions indicated.

the silicon substrate, the diffraction pattern obtained at $\theta_i = 2.3°$ and $\phi = 1°$ off the Si[11$\bar{2}$] zone axis was followed as a function of time (see Figs. 3*C* and 5*B*). At this higher θ_i angle, Bragg spots from the bilayer as well as the silicon substrate can be observed, making the comparison straightforward. The Bragg spots were analyzed in a similar way as for the lower θ_i angles. The change of the lattice constant in the bilayer and silicon as a function of time are shown in Fig. 5*B*. As expected, the LB(002) peak shows the same behavior as in Fig. 5*A*. However, the silicon lattice undergoes a very different dynamics. Whereas the spot LB(002) of the bilayer changes only in the vertical direction, the spots of the silicon also change sideways, indicating a displacement in the planes parallel to the interface. The absolute change in the lattice spacing is much smaller in silicon than in the bilayer, 0.013 vs. 0.072 Å. The temporal behavior indicates the temperature rise, which is similar to the behavior observed before (8); after the rise, the silicon restructures on the nanosecond time scale. The presence of the bilayer on the surface enhances the vibrational couplings (faster rise) (24) and suppresses the large amplitude surface displacement of silicon without the bilayer.

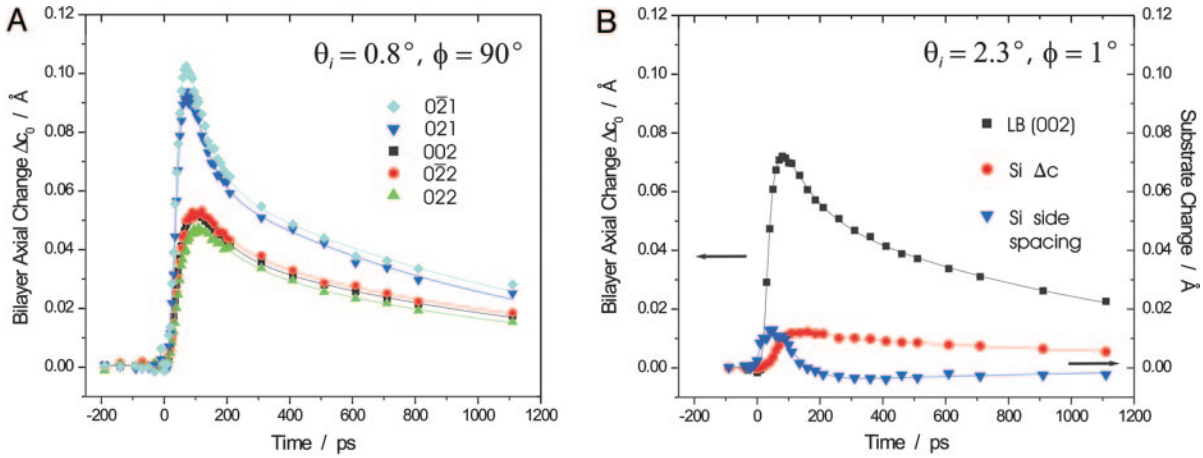

Fig. 5. Structural dynamics of the bilayer. (*A*) The molecular length change Δc_0 of the CH_2 subcell as a function of time for $\theta_i = 0.8°$ and $\phi = 90°$ shows the behavior for the different diffraction spots indexed. (*B*) The change of the CH_2 subcell in the bilayer and of the substrate for $\theta_i = 2.3°$ and $\phi = 1°$. The LB bilayer Δc_0 is obtained from momentum transfer *s*-values of the Bragg spots (002); the Si Δc from *s* of the Bragg spots Si(00); and Si side spacing from *s* of the Bragg spots Si(10) and Si(00). Note the same scale for all of the graphs and the difference in amplitude in *B* between the silicon and bilayer change.

A general dynamical structure picture of the bilayer can now be described as follows. Because there is no absorption resonance for the fatty acids at the wavelength of the heating pulse, the pulse is absorbed only by the substrate and the bilayer is practically transparent. The femtosecond excitation creates electron-hole pairs in silicon and the energy is then transferred to the lattice through electron-phonon coupling in a few ps, as described in our earlier studies on Si and GaAs surfaces (8, 9). The energy is transferred into the bilayer on this ultrashort time scale. However, the expansion in the bilayer is only in the direction perpendicular to the interface, i.e., along the aliphatic chains of the molecules, indicating an efficient and "wire-like" energy transfer within the fatty acid assembly. The covalent bondings in the chains, as opposed to the weak interactions across chains, facilitate such directional motion.

The expansions in the fatty acid bilayer are coherent but anisotropic, reaching the maximum of 0.10 Å, with a time constant of 25 ps. The persistence of diffraction spots with time indicates that disorder in the chains is a small amplitude motion, relative to the bond lengths involved. After reaching maximum expansion, the structure becomes a nonequilibrium state, and energy redistribution in 55 ps drives the system toward equilibration. The remaining contraction toward the initial equilibrium state is dominated by much slower decay on a nanosecond time scale ($\tau \approx 1.15$ ns).

However, the meaning of complete equilibration here must be handled cautiously. At the maximum extension of the fatty acids (0.10 Å) the effective temperature (8, 9) is clearly above the melting point of the assembly (in the range of 100°C), but the structure is far from equilibrium and in modes mainly of the stretch and scissor vibrations of the chains. It would appear that at much longer times the distances may reach those dictated by the values of the thermal expansion coefficient α, in the range of 10^{-4} to 10^{-5} deg^{-1} (25). However, even at the longest time, the diffraction still shows significant positive values of Δc_0. (Only if the rotation of chains is near free can we observe the negative values.) Thus, the transition to the final equilibrium and the effective α can be obtained by studying the complete temperature range of diffraction for a molecular bilayer.

At the atomic-scale level, the motions along the chains should reflect the nonlinear behavior of coupled oscillators, the forming of wave motion by local change in velocity and amplitude. If true, the behavior is that of a soliton-type motion, a spatially localized, coherent motion that is dynamically and structurally stable. Molecular dynamics simulations and theoretical considerations of anharmonically coupled bonds are being examined to elucidate these points. The insensitivity of the distances (perpendicular to the chains) to the heat change is consistent with the reduced interaction between chains compared with in-chain interactions. The influence of stacking is also a major consideration in the condensed phase.

Conclusion

These studies demonstrate the achievement of atomic-scale resolution, spatially and temporally, in determining the structures and dynamics of fatty acid bilayers (≈50 Å) by using UEC. Because of the monolayer sensitivity we are able to observe the dynamical nature of the 2D "crystalline" bilayer, unlike the reported self-assembled monolayer structures (24), and the influence of interfacial order, even for hydrophobic substrates. Moreover, the coherent "soliton-type" and anisotropic expansion of the bilayer may prove general in explaining mechanisms of motion and transport.

We thank Prof. J. Heath for the use of his facilities and Drs. Y. Luo and H. Yu for the preparation of the LB bilayer. This work was supported by the National Science Foundation.

1. Ertl, G. (2000) *Adv. Catal.* **45,** 1–69.
2. Thomas, J. M. (1997) *Chem. Eur. J.* **3,** 1557–1562.
3. Eisenthal, K. B. (1993) *Acc. Chem. Res.* **26,** 636–643.
4. Merz, K. M., Jr. & Roux, B. (1996) *Biological Membranes* (Birkhäuser, Boston).
5. Grell, E. (1981) *Membrane Spectroscopy* (Springer, Berlin).
6. Shinitzky, M. (1993) *Biomembranes: Physical Aspects* (VCH, Weinheim, Germany), Vol. 1.
7. Vendruscolo, M. & Dobson, C. M. (2005) *Philos. Trans. R. Soc. London A* **363,** 433–452.
8. Ruan, C.-Y., Vigliotti, F., Lobastov, V. A., Chen, S. & Zewail, A. H. (2004) *Proc. Natl. Acad. Sci. USA* **101,** 1123–1128.
9. Vigliotti, F., Chen, S., Ruan, C.-Y., Lobastov, V. A. & Zewail, A. H. (2004) *Angew. Chem. Int. Ed.* **43,** 2705–2709.
10. Ruan, C.-Y., Lobastov, V. A., Vigliotti, F., Chen, S. & Zewail, A. H. (2004) *Science* **304,** 80–84.
11. Roberts, G. (1990) *Langmuir-Blodgett Films* (Plenum, New York).
12. Petty, M. C. (1996) *Langmuir-Blodgett Films* (Cambridge Univ. Press, Cambridge).
13. Germer, L. H. & Storks, K. H. (1938) *J. Chem. Phys.* **6,** 280–293.
14. Russell, G. J., Petty, M. C., Peterson, I. R., Roberts, G. G., Lloyd, J. P. & Kan, K. K. (1984) *J. Mat. Sci.* **3,** 25–28.
15. Robinson, I., Jarvis, D. J. & Sambles, J. R. (1991) *J. Phys. D Appl. Phys.* **24,** 347–359.
16. Bürsing, H., Ouw, D., Kundu, S. & Vöhringer, P. (2001) *Phys. Chem. Chem. Phys.* **3**, 2378–2387.
17. Rousse, A., Rischel, C., Uschmann, I., Forster, E., Albouy, P. A., Geindre, J. P., Audebert, P., Gauthier, J. C. & Antonetti, A. (1999) *J. Appl. Crystallogr.* **32**, 977–981.
18. Lobastov, V. A., Srinivasan, R., Vigliotti, F., Ruan, C.-Y., Feenstra, J., Chen, S., Park, S. T., Xu, S. & Zewail, A. H. (2003) in *UltraFast Optics IV*, Springer Series in Optical Sciences, eds. Krausz, F., Korn, G., Corkum, P. & Walmsley, I. (Springer, Berlin), pp. 413–429.
19. Spence, J. C. H., Poon, H. C. & Saldin, D. K. (2004) *Microsc. Microanal.* **10,** 128–133.
20. Kitaigorodskii, A. I. (1961) *Organic Chemical Crystallography* (Consultants Bureau, New York).
21. Schwartz, D. K., Viswannathan, R., Garnaes, J. & Zasadzinski, J. A. (1993) *J. Am. Chem. Soc.* **115**, 7374–7380.
22. Takamoto, D. Y., Aydil, E., Zasadzinski, J. A., Ivanova, A. T., Schwartz, D. K., Yang, T. & Cremer, P. S. (2001) *Science* **293,** 1292–1295.
23. Mahan, J. E., Geib, K. M., Robinson, G. Y. & Long, R. G. (1990) *J. Vac. Sci. Technol. A* **8,** 3692–3700.
24. Ruan, C.-Y., Yang, D.-S. & Zewail, A. H. (2004) *J. Am. Chem. Soc.* **126,** 12797–12799.
25. Fukui, T., Sugi, M. & Iizima, S. (1980) *Phys. Rev. B* **22,** 4898–4899.